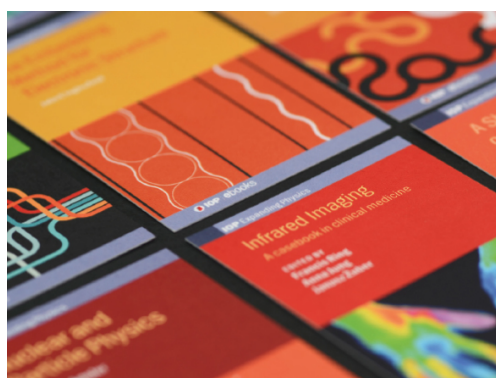**PAPER**

Direct evidence of $E \times B$ flow changes at the onset of resonant magnetic perturbation-driven edge-localized mode crash suppression

To cite this article: Jaehyun Lee *et al* 2019 *Nucl. Fusion* **59** 066033

View the article online for updates and enhancements.

Recent citations

- Pedestal electron collisionality and toroidal rotation during ELM-crash suppression phase under n = 1 RMP in KSTAR
  Minwoo Kim *et al*

- Bifurcation phenomena in magnetically confined toroidal plasmas
  K. Ida

- Edge turbulence characteristics and transport during the ELM mitigation with *n* = 1 resonant magnetic perturbation on EAST
  S.C. Liu *et al*

Direct evidence of $E \times B$ flow changes at the onset of resonant magnetic perturbation-driven edge-localized mode crash suppression

Jaehyun Lee[1], **Y.M. Jeon**[1], **Y. In**[2], **G.Y. Park**[1], **G.S. Yun**[3], **W. Lee**[1],
M. Kim[1], **J.H. Lee**[1], **W.H. Ko**[1], **H.K. Park**[2] and the KSTAR Team

[1] National Fusion Research Institute, Daejeon, 34133, Korea, Republic of
[2] Ulsan National Institute of Science and Technology, Ulsan, 44919, Korea, Republic of
[3] Pohang University of Science and Technology, Pohang, 37673, Korea, Republic of

E-mail: jaehyun@nfri.re.kr

Abstract

The bifurcation of perpendicular mode velocity near the pedestal top ($v_\perp$) at the onset of RMP-driven edge-localized mode (ELM)-crash suppression has been directly measured by using an electron cyclotron emission imaging diagnostic on KSTAR. The ELM crashes are suppressed along with a sudden reduction of $v_\perp$, which synchronizes with the transition into and out of the ELM-crash suppression. The change of $E \times B$ flow appears mainly responsible for the change of $v_\perp$, whose magnitude is the smallest near the normalized flux surface $\Psi_N \sim 0.95$ during the ELM-crash suppression. The plasma response to the RMP field was most enhanced in the vicinity of $\Psi_N \sim 0.95$ during the ELM-crash suppression and showed a hysteresis behavior with respect to resonant field strength. With these changes, a strong nonlinear coupling between turbulent eddies was observed in the ELM-crash suppression, which is an important feature of the ELM-crash suppression.

Keywords: RMP, ELM suppression, turbulence, KSTAR, ECEI

(Some figures may appear in colour only in the online journal)

1. Introduction

The high-confinement mode (H-mode), characterized by the formation of an edge transport barrier (ETB), increases the plasma energy confinement time by about twice as long as the lower-confinement mode [1]. The discovery of the H-mode is considered as one of the most important milestones toward nuclear fusion to satisfy ignition conditions. However, the steep pressure gradient and associated high current density of the ETB lead to a series of bursts of magnetohydrodynamic instabilities referred to as the edge-localized modes (ELMs) [2–4]. Such ELM crashes generally degrade particle and energy confinement up to 20%, damaging the plasma facing components by expelling enormous heat and particle fluxes [5, 6]. One of the promising active methods of ELM control is to perturb the plasma edge with resonant non-axisymmetric magnetic fields, thereby enhancing particle transport and keeping the edge pressure gradient below the threshold of ELM crash. This method, called resonant magnetic perturbation (RMP), has been proven to be effective in several tokamaks [7–10, 14].

Despite the successful ELM crash controls, the understanding of the ELM-crash suppression mechanism is far from perfect yet. The lack of understanding of ELM-crash suppression with the RMP raises the question of the reliability of the RMP-ELM control for ITER. In this respect, the present studies of ELM-crash suppression by the RMP have focused on the plasma response to static RMPs based on nonlinear magnetohydrodynamic (MHD) theory and modeling, and have shown that the plasma flow plays an important role in plasma response to RMP with respect to the ELM-crash

suppression [11, 12]. Notably, various simulations and theories suggest that the electron flow ($v_{\perp,e} = v_{E \times B} + v_e^*$) of plasma across the field lines at the rational flux surfaces determines the level of field penetration. However, it is not yet clear which of the electron flow components is more important for the ELM-crash suppression: $E \times B$ velocity ($v_{E \times B}$) or electron diamagnetic velocity (v_e^*).

On the Korea Superconducting Tokamak Advanced Research (KSTAR), a set of in-vessel magnetic perturbation coils was installed to suppress ELM crashes in H-mode plasmas in 2010 [13]. The KSTAR has a set of 12 coils at the outboard side wall, consisting of four top coils, four middle coils, and four bottom coils. Each coil has two turns and creates a radial magnetic field with toroidal mode number $n = 1$ or $n = 2$ with a variety of coil configurations.

In this work, it is demonstrated that the changes of perpendicular flow are well correlated with the onset of the ELM-crash suppression on the KSTAR tokamak. An electron cyclotron emission imaging (ECEI) system was used for this study, and a detailed description of the system is given in section 2. The perpendicular flow of the plasma was measured by tracking the movement of turbulent eddies (section 3). Detailed observations such as changes in the perpendicular flow before and during the ELM-crash suppression and the types of measured plasma flow are described in section 4. Normalizing the observed perpendicular flow change can visualize more efficiently the plasma response to magnetic perturbation. Using this, section 5 describes in detail the strong plasma response in the ELM-crash suppression and the hysteresis behavior of plasmas for magnetic perturbation. In section 6, bicoherence analysis was conducted to investigate the effect of the perpendicular flow change on the characteristics of turbulence during the transition of the ELM-crash suppression. The global effect of perpendicular flow changes is discussed in section 7, and the summary and conclusions are given in section 8.

2. ECEI at KSTAR

The ECEI can be simply regarded as a microwave camera for 2D electron temperature fluctuation measurements. The ECEI measures the electron emission temperature fluctuations ($\tilde{T}_{ECE} = \delta T_{ECE} / \langle T_{ECE} \rangle$, where $\delta T_{ECE} = T_{ECE} - \langle T_{ECE} \rangle$ and $\langle T_{ECE} \rangle$ is a time average) in the plasma poloidal cross-section, providing unique information on the ELM dynamics not available from conventional diagnostics. Up to now, the ECEI systems have played a crucial role in studying turbulence physics [15, 16] as well as core MHD physics [17, 18].

The KSTAR ECEI system has dual independent heterodyne detector arrays, which allow simultaneous measurement of the inboard and outboard side [19, 20]. With the flexible large-aperture optics, the two views of the ECEI system can be focused anywhere in the poloidal cross-section and the vertical coverage can be varied from 30–90 cm. Each detector array consists of total 24 (vertical) × 8 (radial) = 192 channels with a spatial resolution of 1–2 cm^2 and a temporal resolution of 2 μs. The detector arrays of the KSTAR ECEI system are optimized to detect the extraordinary mode second harmonic (X2-mode) ECE in the frequency range of
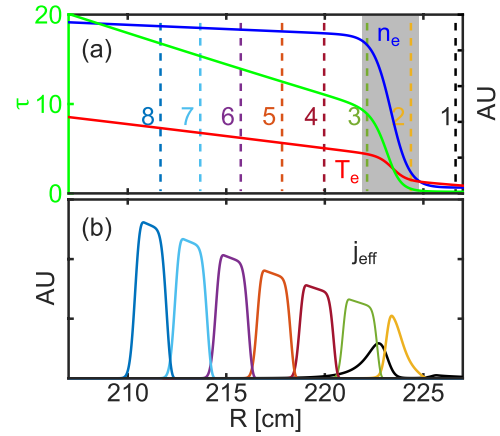

Figure 1. (*a*) The optical thickness profile (green) calculated with T_e (red) and n_e (blue) profiles for the typical KSTAR H-mode discharge. (*b*) Example of the spatial profiles of emission arriving at the eight midplane channels of ECEI. The dotted lines are the cold resonance positions of the center frequencies of the ECEI channels. When the diagnostic channel has a cold resonance outside the steep gradient region ($\Psi_N \sim 1$), such as channel 1, the emission position is far from the cold resonance position.

75–140 GHz, which is a linearly polarized wave perpendicular to the magnetic field. For high field operations $B_0 > 3$ T, the ordinary mode fundamental (O1-mode) ECE can be used with a large-aperture polarization rotator because the X2-mode ECE exceeds the detectable frequency range [21].

For reliable ECE measurements, the optical thickness (τ) of the plasma should be much greater than 1 in measured region. In practice, if $\tau > 3$, the most radiation from the source is absorbed, and the plasma can be regarded as optically thick. For the optically thick plasma, the intensity of the ECE radiation can be interpreted as the local T_e. Whereas if $\tau < 3$, the ECE measurements are affected by n_e and the measured radiation is no longer the real T_e of the plasma. By integrating the local ECE intensity over the frequency, a spatial profile of emission intensity measured at each diagnostic channel can be plotted (figure 1). This analysis uses the characteristics of the eight midplane channels of the ECEI diagnostic with a typical example of the KSTAR H-mode discharge. Inside the pedestal top, the ECE is considered to be local and optically thick, which means that the ECE can respond with the local $\tilde{T}_e$. However, the ECE intensity spectrum outside the steep gradient region (or scrape-off layer (SOL)), such as channel 1, is relativistically downshifted emission that originates not in the SOL, but inside the steep gradient region (the gray area in figure 1(*a*)). Such ECE may be optically gray and may have no direct correlation to the local T_e. Note that the KSTAR ECEI system does not provide imaging on the outside of the separatrix, in which the local ECE measurement is no longer valid. The coherent movement of the ELM filaments with the high contrast image from the ECEI system is a good evidence of the localization of ECE [22].

3. Perpendicular mode velocity measurement using ECEI

The perpendicular mode velocity ($v_\perp$) can be derived from the experimentally measured turbulent fluctuations using the
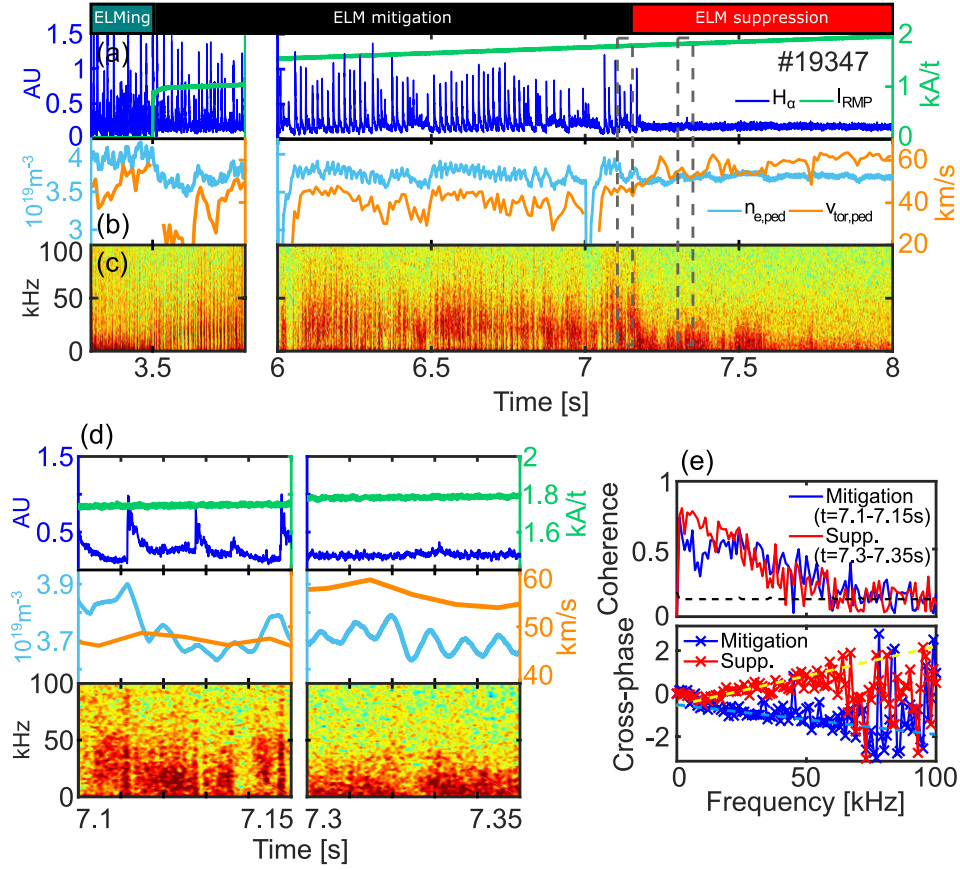
Figure 2. (*a*) Time history of H_α signal (blue) with RMP coil current I_{RMP} (green). (*b*) Electron density (blue) and toroidal rotation in the co-current direction (yellow) near the pedestal top ($\Psi_N \sim 0.95$). (*c*) Spectrogram of ECEI signal located in the vicinity of the ELM filament (or edge turbulent eddies). (*d*) Zoom-in figures of the area marked by the gray dotted box. (*e*) Coherence and cross-phase calculation using two adjacent ECEI channels in the poloidal direction. The black dashed line in the coherence plot is the statistical error limit. The reference lines in the cross-phase plot are the linear fitting result considering the coherence weighting.

correlation method. The ECEI system has been used to measure the turbulent fluctuations at the plasma edge. The velocity of modes in the ECEI view (dubbed as pattern velocity v_{pt}) can be written in terms of mode pitch as

$$v_{pt} = v_\perp / \cos \alpha_*, \tag{1}$$

where the α_* is pitch angle near the midplane [17, 23]. The parallel velocity ($v_\parallel$) contribution can be negligible to the pattern velocity of turbulent eddies in the lab frame since the turbulent eddies are highly elongated along the magnetic field lines, i.e. $k_\perp v_\perp / k_\parallel v_\parallel \gg 1$. In general, the pattern velocity of turbulent eddies at the edge represents the perpendicular flow velocity effectively since α_* is quite small ($\cos \alpha_* \approx 1$). The phase-slope method based on the cross-phase analysis is applied to quantify the $v_\perp$ using multichannel ECEI data [16, 24]. For example, the cross-phase from two adjacent ECEI channels allows us to produce an averaged group velocity from the spatial separation of the channels Δz and a phase-slope $m = \Delta\phi / \Delta f$: $v_\perp = \Delta\omega / \Delta k = 2\pi \Delta z / m$. This method is suitable for the ECEI data set, which has a high time resolution with limited spatial resolution.

4. KSTAR experiments for evaluating the effect of perpendicular flow

4.1. Perpendicular mode velocity changes at the transition of ELM-crash suppression

Typical ELM-crash suppressed H-mode plasmas in KSTAR have lower single null diverted configurations with high elongation $\kappa \geqslant 1.7$ and triangularity $\delta \geqslant 0.5$. These discharges have been operated with the toroidal magnetic field of $B_t = 1.8$–2.0 T in the co-current direction, plasma current of $I_p \approx 0.5$–0.8 MA, and the corresponding edge safety factor $q_{95} \approx 4$ or 5 for $n = 1$ RMP and $q_{95} \approx 3.4$ or 3.8 for $n = 2$ RMP. In these experiments, the RMP field strength was slowly varied in order to clarify the detailed dynamics of the ELM-crash suppression. An example of the ELM-crash suppression under slow varying RMP field ($n = 1$, $+90°$ phasing) is illustrated in figure 2. Upon the application of the RMP field ($t = 3.5$ s), both pedestal electron density and toroidal rotation near the pedestal top drop sharply, and the amplitude of ELM crash in H_α signal is slightly reduced. Then, the ELM crashes suddenly disappear entirely from the H_α signal ($t \sim 7.2$ s)

when the perturbing field strength exceeds a certain threshold. Note that abrupt signal excursions around $t \sim 6$ and 7 s are due to the neutral beam modulation for rotation measurement. At the same time, the ECEI channels often show broadband fluctuations along with the ELM filaments. Recent research work reported that strong interaction between the ELM filament and broadband fluctuations presumably induced by RMP played an important role in the ELM-crash suppression [15, 25].

Correlation analyses between ECEI channels were performed to measure small-scale broadband fluctuations under the RMP field. For KSTAR ECEI, the upper bound of the measurable wave number is $k_\perp \leqslant 1.2$ cm^{-1} at the plasma edge. This range covers long wavelength turbulence such as the kinetic ballooning mode, microtearing mode, ion temperature gradient, etc. Since long time averaging is required for reliable correlation analyses, nearly stationary plasma conditions are considered (i.e. time at $t = 6$–8 s, pedestal electron density $n_{e,ped} \sim 3.7 \times 10^{19}$ m^{-3}, and toroidal rotation of carbon impurity at the pedestal top $v_{tor,ped} = 40$–60 km s^{-1}). Figure 2(*e*) is an example of the plasma turbulence measurement with the coherence and cross-phase techniques using the vertically separated ECEI channels in the pedestal region. The plasma state under the RMP field is characterized by the small-scale broadband turbulent fluctuations ($f < 70$ kHz) along the vertical direction in the pedestal region [15, 26]. The peak frequency of turbulent fluctuations decreases in the ELM-crash suppressed phase and the peak value increases slightly compared to the ELM-crash mitigated phase. This implies that the turbulent fluctuation level increases after the transition to the ELM-crash suppression phase, and the velocity of turbulent modes in the ECEI view, expressed as the slope of the cross-phase, changes dramatically. Note that the turbulence measurement in the ELM-crash mitigated phase was performed except for the ELM crash and the measurable fluctuation level of $\tilde{T}_{ECE}/T_{ECE}$ is ~0.25% through the correlation over $\Delta t = 0.1$ s (with intermediate frequency bandwidth of 600 MHz and video bandwidth of 400 kHz). Inherent thermal noise cannot contribute to a real correlation between well-separated channels in space.

Figure 3(*a*) is the time evolution of the $v_\perp$ near the pedestal top at the transition to the ELM-crash suppression. The $v_\perp$ estimated by the rotation of turbulent eddies has a value of ~10 km s^{-1} along the electron diamagnetic direction during the ELM-crash mitigated phase. Note that the error bars represent the standard deviation in the slope fitting with 95% confidence bounds and the velocity resolution is limited by the time resolution of ECEI. High $v_\perp \geqslant 10$ km s^{-1} would prevent the penetration of externally-applied resonant perturbing field into plasma, leading to an effective screening of RMPs [27–29]. As the RMP field strength increases slightly above a threshold, the plasma edge is altered to the ELM-crash suppressed state, coincident with the bifurcation of $v_\perp$. The change of $v_\perp$ occurs faster than ~100 ms near the onset of ELM-crash suppression, and the bifurcated $v_\perp$ in the ELM-crash suppressed phase is typically small on the order of ~1 km s^{-1}. Figure 3(*b*) is the reversed process, which is
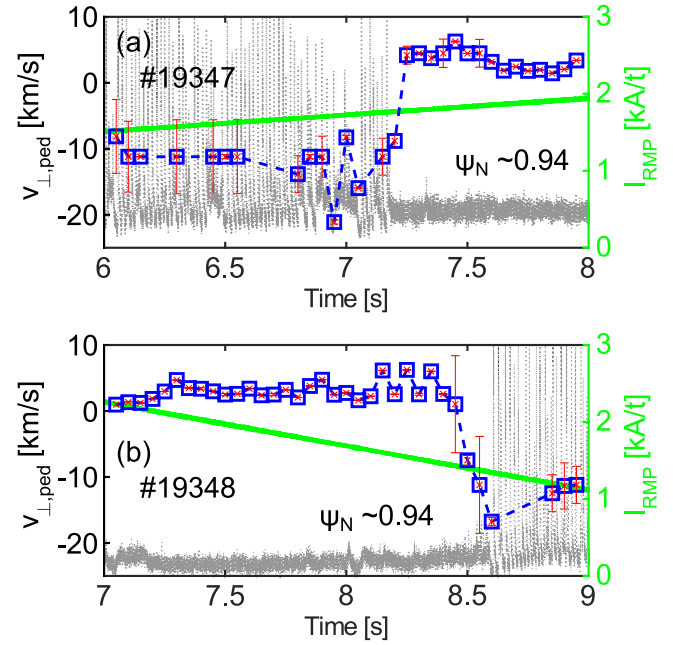

Figure 3. Time trace of perpendicular plasma flow near the pedestal $v_\perp$ ($\Psi_N \approx 0.94$) with slowly (*a*) increasing and (*b*) decreasing RMP field strength respectively.

the transition from the ELM-crash suppression to mitigation. Overall, the bifurcation of $v_\perp$ synchronizes with the transition into and out of ELM-crash suppression, strongly suggesting that the change of $v_\perp$ could be directly associated with the ELM-crash phase transition [30].

4.2. Physical meaning of perpendicular mode velocity measured by ECEI

Interpreting the physical meaning of the measured $v_\perp$ can play an important role in understanding of the ELM-crash suppression mechanism. The measured $v_\perp$ from the turbulent fluctuations contains two components: $v_\perp = v_{E \times B} + v_{ph}$ [24]. The separation of the two components is not straightforward and requires the help of numerical simulation as well as experimental measurements. The linear drift-wave theory, which is the simplest approach to estimate the v_{ph} of dominant drift-wave turbulence yields that v_{ph} is roughly given by the $v_e^*(= T_e/L_n B$, where L_n is the density scale length $|n/n'|$) [31–33].

Figures 4(*a*) and (*b*) show edge T_e and n_e profiles measured by a Thomson scattering (TS) system in the ELM-crash mitigated and suppressed phases. A modified hyperbolic tangent function with Gaussian function is used for fitting the edge profiles [34]. The TS profiles in the ELM-crash mitigation were obtained using 50%–99% of the inter-ELM crash period to reduce the impact of the ELM crash [35, 36], and the estimates of profile uncertainties that could affect the calculation are expressed as line thickness. The pedestal temperature $T_{e,ped}$ decreases by ~20% and the gradient of the pedestal density $\nabla n_{e,ped}$ increases by ~15% after the transition of the ELM-crash suppression. Although both the $T_{e,ped}$ and $\nabla n_{e,ped}$

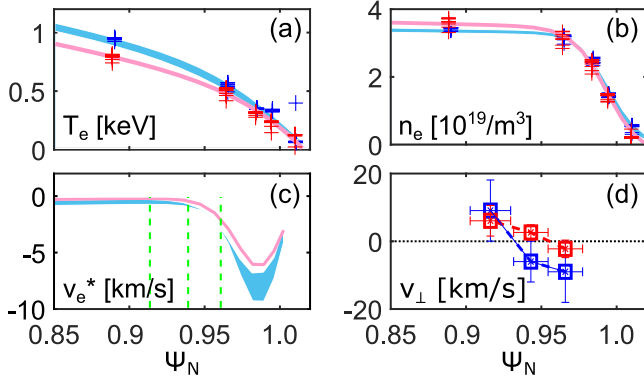**Figure 4.** (*a*) Electron temperature T_e, (*b*) electron density n_e, (*c*) electron diamagnetic flow v_e^*, and (*d*) local perpendicular flow $v_\perp$ profiles as function of the normalized poloidal flux Ψ_N before (blue) and during the ELM-crash suppression (red). The green vertical lines in (*c*) correspond to the ECEI channel positions where the $v_\perp$ is measured.

Figure 5. The averaged (*a*) T_e and (*b*) n_e from an H-mode (#18594) as measured by TS, (*c*) the toroidal (yellow) and poloidal (green) rotation as measured by CES. (*d*) The comparison between the calculated $E \times B$ rotation profile based on the radial force balance equation and the $v_\perp$ measured by ECEI.

profiles changed after the transition to the ELM-crash suppression, the two effects complement each other and thus there are no significant change in the v_e^*; the v_e^* increased by less than 1 km s^{-1} in the electron diamagnetic direction at the measurement position (figure 4(*c*)). The change of local $v_\perp$ profile measured by the ECEI is approximately 10 km s^{-1}, which occurs suddenly for $\sim$100 ms near the onset of the ELM-crash suppression (figure 4(*d*)). These observations suggest that the $v_{E \times B}$ mainly contributes to the $v_\perp$ measured by the ECEI and the change of $v_{E \times B}$ causes the $v_\perp$ bifurcation. In many cases, the v_{ph} is very small compared to $v_{E \times B}$ [23, 32, 33], and it is considered that there is no change of the turbulence type because the wave number of the measured turbulence does not change much before and during the ELM-crash suppression (figure 2(*e*)). The measurement of $v_\perp$ profile also shows the decrease of $v_\perp$ shear locally, which could lead to the increase of turbulent fluctuations at the edge in the ELM-crash suppressed phase [15, 25, 30]. Such turbulent fluctuations occur near the pedestal top and the magnitude of $v_\perp$ is the smallest near the $\Psi_N \sim 0.95$. Note that the measurement location of the ECEI, marked by the green line, was determined by considering both poloidal magnetic field (B_p) and relativistic shift effect, which affect the ECE resonance position (figure 4(*c*)).

In order to verify this result, the $v_{E \times B}$ calculated from the profiles and the $v_\perp$ estimated from ECEI were compared in the ELMy H-mode discharge. Since the KSTAR poloidal charge exchange recombination spectroscopy (CES) was not routinely operated in this experimental campaign, the $v_{E \times B}$ was calculated at a specific discharge (#18594) which can use all profile data needed for the radial force balance equation: $v_{E \times B} = (Z_j e n_j B)^{-1} \nabla p_j - v_{pol} B_{tor}/B + v_{tor} B_{pol}/B$. Here, Z_j is the ion charge, n_j is the ion density, e is the electron charge, p_j is ion pressure, and B_{tor} and B_{pol} are the toroidal and poloidal magnetic fields, respectively. Figure 5(*d*) illustrates the comparison between the turbulence pattern velocity measured by ECEI (pink squares) and the $E \times B$ velocity calculated from the radial force balance equation (red). The T_e, n_e, and poloidal/toroidal rotation profiles measured with the TS and the poloidal/toroidal CES were used (figures 5(*a*)–(*c*)). The
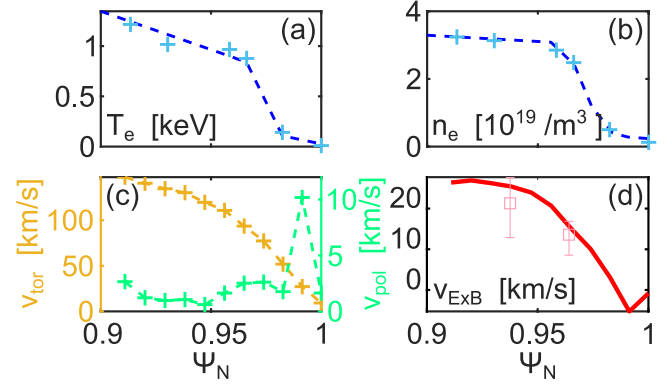
profiles were obtained by averaging the data from the inter-ELM crash period, similar to the figure 4. Good agreement is found between the measured turbulence pattern velocity and the $E \times B$ velocity within the error bars. Though not the same ELM-crash suppressed plasma, this could be another supporting evidence that the motion of broadband turbulence is dominated by the $E \times B$ flow.

5. Plasma response to RMP

The RMP field strength dependence can be understood by investigating the slower $v_\perp$ that has a larger plasma response [37]. In this case, for a systematic analysis, the $v_\perp$ is calculated using time delay estimation [38, 39], which gives a similar result as the phase-slope method. Figure 6 is the temporal evolution of $v_\perp$ normalized to the maximum and minimum values of each channel ($v_{\perp,N}$) at the transition into and out of the ELM-crash suppression: $v_{\perp,N} = (v_\perp - v_{\perp,min})/(v_{\perp,max} - v_{\perp,min})$ for $|v_{\perp,miti}| \geqslant |v_{\perp,supp}|$ and $v_{\perp,N} = (v_\perp - v_{\perp,max})/(v_{\perp,min} - v_{\perp,max})$ for $|v_{\perp,miti}| < |v_{\perp,supp}|$, where $v_{\perp,max}$ and $v_{\perp,min}$ are the maximum and minimum $v_\perp$ of each channel. The normalized $v_\perp$ response to $n = 1$ RMP suddenly increases in the vicinity of the $\Psi_N \sim 0.95$ near the onset of the ELM-crash suppression and persists while the ELM crashes are suppressed (figure 6(*a*)). The $v_\perp$ response driven by the RMP is spatially localized and precedes the ELM dynamics change. This is in contrast to the weak response of $v_\perp$ observed inside the $\Psi_N \sim 0.95$ in the ELM-crash mitigated phase. Note that the weak response of $v_\perp$ comes from the fast $v_\perp$ or weak turbulent fluctuations. These strong plasma responses are also confirmed in the lower q_{95} ELM-crash suppression, in which the $n = 2$ RMP field strength is kept constant ($I_{RMP} = 2.95$ kA t^{-1}) but the q_{95} is varied (figure 6(*c*)). Note that the position at which the strong $v_\perp$ response appears, slowly changes due to the increase of B_p with increasing I_p. The measurements show that the most responsive rational flux surface for the ELM-crash suppression is $\Psi_N \sim 0.95$, and the ELM crashes are suppressed when the $v_\perp$ response is strongly sustained at this location. Thus, keeping $v_\perp$ to a small value at the q_{95} rational surface could play an
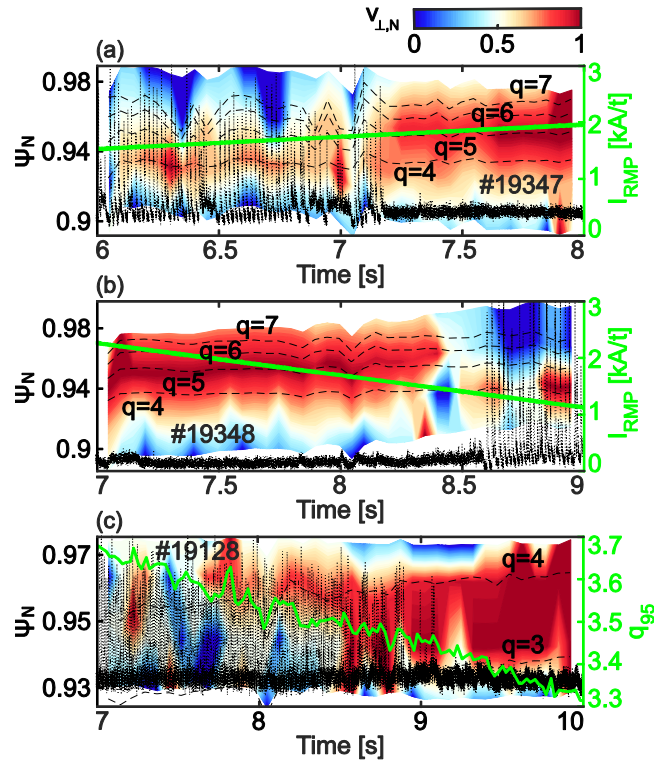
Figure 6. Contours of 'normalized' $v_\perp$ versus time and Ψ_N in the transition into and out of ELM-crash suppression overlaid with H_α signal. (*a*) A transition from ELM-crash mitigation to suppression with slowly increasing RMP field for the discharge #19347. (*b*) A transition from ELM-crash suppression to mitigation with slowly decreasing RMP field for the discharge #19348. (*c*) A transition from ELM-crash mitigation to suppression with slowly varying q_{95} under constant RMP field strength for the discharge #19128.

important role in suppressing ELM crashes, which could have benefited from a strong plasma response to the RMP.

In a related experiment, the hysteresis in the resonant field strength was thoroughly investigated at the transition into and out of the ELM-crash suppression. The RMP coil current was slowly increased and decreased in a single discharge, as shown in figure 7(*a*). The RMP field strengths for the transition were quite different, when entering and exiting the ELM-crash suppression; the RMP coil current was ~30% (~0.5 kA t^{-1}) higher at the entering phase to the ELM-crash suppression than at the exiting phase to the ELM-crash mitigation. It also shows the time evolution of the $v_\perp$ before, during, and after the RMP induced ELM-crash suppression. The $v_\perp$, which was hardly responding to the RMP field at the initial phase, suddenly decreases after exceeding the threshold. The reduced $v_\perp$ was sustained during the ELM-crash suppression and returned back to its original level when the ELM crashes reappeared. The hysteresis can be seen more explicitly through a hysteresis loop by plotting $v_\perp$ as a function of I_{RMP} as shown in figure 7(*b*). Such hysteresis suggests that the ELM-crash suppression can be sustained even after reducing RMP field strength if the ELM crashes are suppressed, and RMP coil current can be optimized to improve plasma performance during the ELM-crash suppression. These observations are quite analogous to nonlinear modeling of forced magnetic reconnection based on the balance
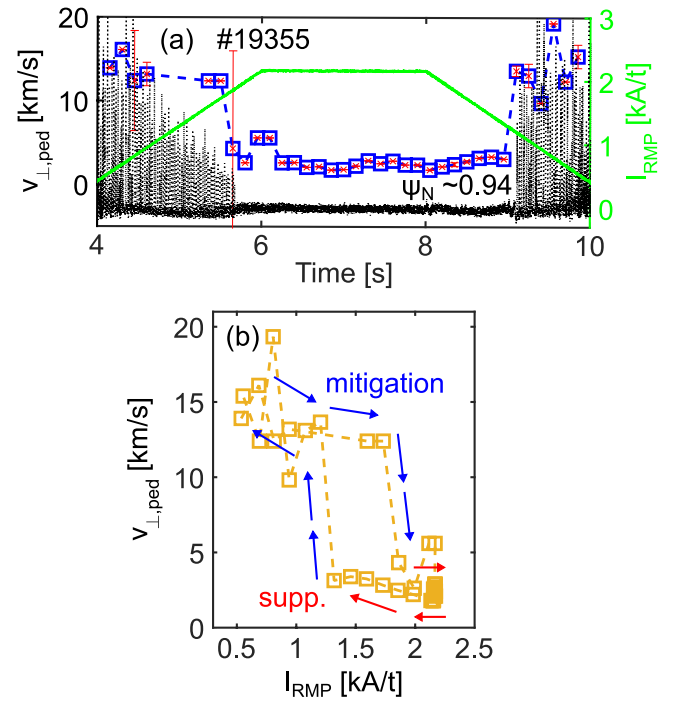

Figure 7. (*a*) The ELM phase transition and $v_\perp$ change with the RMP field strength. (*b*) Hysteresis loop in transition into and out of the ELM-crash suppression.

between electromagnetic and viscous forces [40, 41]. As the perturbing field is increased, the plasma state bifurcates to a state having a slow rotation and a large magnetic island. These changes could affect the pedestal stability by heat/particle transport due to the RMP field penetration to the plasma and the resulting turbulent fluctuations, and thereby keep the pressure gradient below the threshold of the ELM crash [15].

6. Nonlinear coupling between turbulent eddies

Turbulent fluctuations immediately occur upon application of RMP regardless of the ELM-crash suppression and tend to increase with the RMP field strength during the ELM-mitigated phase. If the RMP induces the turbulent fluctuations and the turbulent fluctuations are related to the ELM-crash suppression, the question arises, what is the difference between ELM-crash mitigation and suppression in terms of turbulent fluctuations. One possible candidate for explaining the difference is a nonlinear coupling process between turbulent eddies (or ELM filament and turbulent eddies). The nonlinear coupling between various fluctuation modes can usually be calculated by bicoherence and is given by

$$b^2(t, f_1, f_2) = \frac{|\langle F(f_1)F(f_2)F^*(f_1+f_2)\rangle|^2}{\langle |F(f_1)F(f_2)|^2\rangle\langle |F^*(f_1+f_2)|^2\rangle}, \quad (2)$$

where b is the bicoherence evaluated with f_1 and f_2, F is the Fourier transform of the signal, and $\langle\cdot\rangle$ denote ensemble averaging [42]. The bicoherence typically yields information on the degree of phase coupling, which is a requirement for nonlinear interactions. Figure 8 is the bicoherence of ECEI signal located in the vicinity of the $\Psi_N \sim 0.95$ in the ELM-crash mitigated phase and the ELM-crash suppressed phase. In both
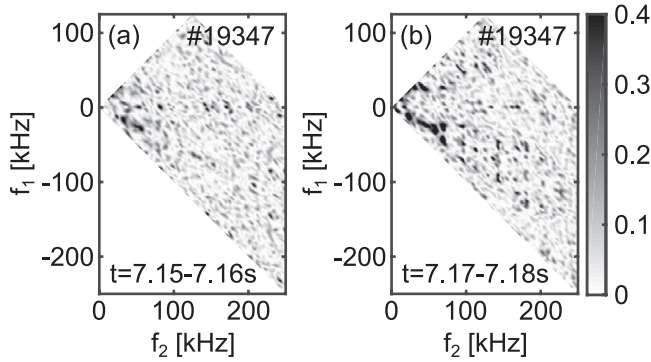
Figure 8. Bicoherence during (*a*) the ELM-crash mitigated phase and (*b*) the ELM-crash suppressed phase.
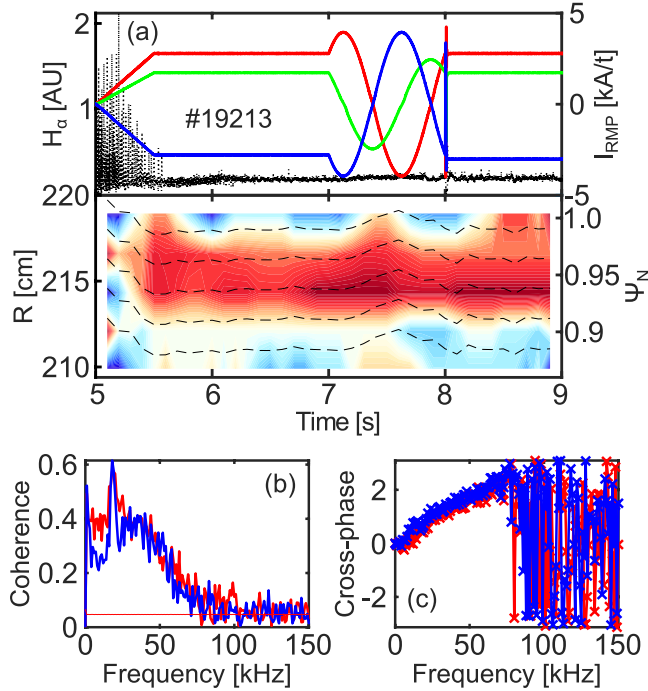

Figure 9. (*a*) 2D contour plot of normalized $v_\perp$ with rigidly rotating RMP field: coil current of upper(blue)/middle(green)/lower(red) RMP to indicate the time period of the rigid rotation. The black dashed lines show the normalized flux surfaces estimated by magnetic equilibrium. (*b*) Coherence and (*c*) cross-phase measurement with respect to the RMP coil phase. The blue ($t = 7.2$–7.5 s) and red ($t = 7.65$–7.95 s) lines correspond to the radially inner and outer perturbation fields of the middle coil, respectively.

cases, low-frequency modes are nonlinearly active. During the ELM-crash mitigation phase as shown in figure 8(*a*), the nonlinear interaction is dominated by coupling of turbulent fluctuations in the range of 20–70 kHz but the amplitude of bicoherence is weaker. The weak coupling between turbulent fluctuations suggests that there is little interaction between turbulent eddies, which may be due to the change of flow shear [43]. In the ELM-crash suppression phase (figure 8(*b*)), on the other hand, the 20–70 kHz fluctuations couple with each other similar to the ELM-crash mitigation, but a low-frequency fluctuation is also observed. As a result, the main difference between the ELM-crash mitigation and suppression is the existence of low-frequency turbulent fluctuation coupling

and the strong nonlinear coupling between the turbulent fluctuations below 70 kHz. These strong nonlinear interactions may lead to prevention of the growth of the most dominant instability through the energy exchange and make the plasma stay in a metastable state for the ELM crashes. It is expected that this nonlinear coupling is related to the change of the $v_\perp$ or its shear at the onset of ELM-crash suppression; this will be the topic of future experiments and analysis.

7. Discussion

Recent experimental results have shown that the 3D effect by RMP can be different depending on the toroidal position of the plasma [44–47]. In this work, the $v_\perp$ was measured at a fixed toroidal position where the ECEI is located, so the 3D effect by RMP was not taken into account. This raises the question of whether the bifurcation of $v_\perp$ is a global phenomenon or a toroidally local phenomenon. For the KSTAR, radial displacement of plasma by RMP is ~ 1 cm, which may change the separatrix position depending on the toroidal phase. Figure 9(*a*) is the 2D contour plot of normalized $v_\perp$ in an ELM-crash suppressed plasma with a rigid rotating $n = 1$ RMP. Due to the RMP rotation, the plasma flux surfaces were slightly perturbed ($\Delta\Psi_N \sim 0.02$) but the strong plasma response represented by normalized $v_\perp$ was maintained in the real space. This may be because the plasma displacement by the RMP is smaller than the radial spatial resolution of the ECEI ($\Delta R \sim 2$ cm for $B_t = 1.8$ T) and thus the change is not measured. In this plasma, the $\Delta\Psi_N \sim 0.02$ by the RMP rotation caused a radial displacement of ~ 1 cm. Otherwise, the region where the turbulence is measured is near the pedestal top, so the 3D effect may be smaller than what the equilibrium evaluates [44, 47]. There is also no significant difference in the cross-phase with respect to the phase changes in the ELM-crash suppressed plasma (figure 9(*c*)). Therefore, it can be concluded that the radial displacement occurs according to the RMP phase, but the effect of RMP phase is not so large in the $v_\perp$ estimation. It means that the bifurcation of $v_\perp$ may be a global effect and the plasma response evaluated by normalized $v_\perp$ is robust during the ELM-crash suppressed phase. Nevertheless, the fact that turbulence and transport characteristics can be different with respect to RMP phase is considered to be an important issue to be confirmed in the future [44, 45].

8. Summary

The onset of ELM-crash suppression under the low-n RMPs is characterized by the sudden reduction of $v_\perp$ and its shear as well as increase of turbulent fluctuations. The bifurcation of $v_\perp$ is synchronized with the transition into and out of ELM-crash suppression. The profile change of T_e and n_e before and during the ELM-crash suppression was too small to explain the significant change of $v_\perp$. These observations indicate that the change in $v_{E\times B}$ is the main contribution to the $v_\perp$ bifurcation and the $v_\perp$ has the smallest value on the $\Psi_N \sim 0.95$ during the ELM-crash suppression. The changes in the normalized $v_\perp$ show the stronger plasma response in the vicinity

of the $\Psi_N \sim 0.95$ throughout the ELM-crash suppression. The ELM-crash suppression induced by the RMP shows a hysteresis behavior with respect to resonant field strength. The non-linear interaction between turbulent eddies is observed to be enhanced in the ELM-crash suppression. This may mean that the energy exchange between the turbulent eddies prevents the growth of the dominant mode such as ELM filaments. Future work will be required for a better understanding of why and how the $v_\perp$ changes suddenly and finding the way to sustain the ELM-crash suppression for a long time by controlling the $v_\perp$ of the plasma. It is expected that the answer to this question can be found through the analysis of the correlation between the turbulent fluctuations and the $v_\perp$ change using advanced imaging diagnostics such as ECEI in future.

Acknowledgments

ORCID iDs

Jaehyun Lee ⓘ https://orcid.org/0000-0002-0852-8817
Y. In ⓘ https://orcid.org/0000-0002-9219-1304
G.S. Yun ⓘ https://orcid.org/0000-0002-1880-5865
W. Lee ⓘ https://orcid.org/0000-0001-6856-3377
M. Kim ⓘ https://orcid.org/0000-0002-8627-4584

References

[1] Wagner F. *et al* 1982 Regime of improved confinement and high beta in neutral-beam-heated divertor discharges of the ASDEX tokamak *Phys. Rev. Lett.* **49** 1408

[2] Connor J.W. 1998 Edge-localized modes—physics and theory *Plasma Phys. Control. Fusion* **40** 531

[3] Suttrop W. 2000 The physics of large and small edge localized modes *Plasma Phys. Control. Fusion* **42** A1

[4] Snyder P.B., Wilson H.R., Ferron J.R., Lao L.L., Leonard A.W., Osborne T.H., Turnbull A.D., Mossessian D., Murakami M. and Xu X.Q. 2002 Edge localized modes and the pedestal: a model based on coupled peeling-ballooning modes *Phys. Plasmas* **9** 2037–43

[5] Loarte A. *et al* 2003 Characteristics of type I ELM energy and particle losses in existing devices and their extrapolation to ITER *Plasma Phys. Control. Fusion* **45** 1549

[6] Leonard A.W. *et al* 1999 The impact of ELMs on the ITER divertor *J. Nucl. Mater.* **266** 109–17

[7] Evans T.E. *et al* 2004 Suppression of large edge-localized modes in high-confinement DIII-D plasmas with a stochastic magnetic boundary *Phys. Rev. Lett.* **92** 235003

[8] Liang Y. *et al* 2007 Active control of type-I edge-localized modes with $n = 1$ perturbation fields in the JET tokamak *Phys. Rev. Lett.* **98** 265004

[9] Kirk A. *et al* 2010 Resonant magnetic perturbation experiments on MAST using external and internal coils for ELM control *Nucl. Fusion* **50** 034008

[10] Suttrop W. *et al* 2011 First observation of edge localized modes mitigation with resonant and nonresonant magnetic perturbations in ASDEX Upgrade *Phys. Rev. Lett.* **106** 225004

[11] Nazikian R. *et al* 2015 Pedestal bifurcation and resonant field penetration at the threshold of edge-localized mode suppression in the DIII-D tokamak *Phys. Rev. Lett.* **114** 105002

[12] Moyer R.A. *et al* 2017 Validation of the model for ELM suppression with 3D magnetic fields using low torque ITER baseline scenario discharges in DIII-D *Phys. Plasmas* **24** 102501

[13] Kim H.K., Yang H.L., Kim G.H., Kim J.Y., Jhang H., Bak J.S. and Lee G.S. 2009 Design features of the KSTAR in-vessel control coils *Fusion Eng. Des.* **84** 1029–32

[14] Jeon Y.M. *et al* 2012 Suppression of edge localized modes in high-confinement KSTAR plasmas by nonaxisymmetric magnetic perturbations *Phys. Rev. Lett.* **109** 035004

[15] Lee J., Yun G.S., Choi M.J., Kwon J.M., Jeon Y.M., Lee W., Luhmann N.C.Jr. and Park H.K. 2016 Nonlinear interaction of edge-localized modes and turbulent eddies in toroidal plasma under magnetic perturbation *Phys. Rev. Lett.* **117** 075001

[16] Choi M.J. *et al* 2017 Multiscale interaction between a large scale magnetic island and small scale turbulence *Nucl. Fusion* **57** 126058

[17] Lee J.E. *et al* 2017 Solitary perturbations in the steep boundary of magnetized toroidal plasma *Sci. Rep.* **7** 45075

[18] Choe G.H., Yun G.S., Park H.K. and Jeong J.H. 2018 Slow crash in modified sawtooth patterns driven by localized electron cyclotron heating and current drive in KSTAR *Nucl. Fusion* **58** 106038

[19] Yun G.S. *et al* 2010 Development of KSTAR ECE imaging system for measurement of temperature fluctuations and edge density fluctuations *Rev. Sci. Instrum.* **81** 10D930

[20] Yun G.S. *et al* 2014 Quasi 3D ECE imaging system for study of MHD instabilities in KSTAR *Rev. Sci. Instrum.* **85** 11D820

[21] Lee J., Yun G.S., Kim M., Lee W. and Park H.K. 2012 Large-aperture broadband polarization rotator for the KSTAR ECE imaging system *J. Instrum.* **7** C01037

[22] Yun G.S., Choi M.J., Lee W., Park H.K., Domier C.W. and Luhmann N.C.Jr. 2012 High contrast 2D visualization of edge plasma instabilities by ECE imaging *J. Instrum.* **7** C01024

[23] Lee W. *et al* 2016 E × B flow velocity deduced from the poloidal motion of fluctuation patterns in neutral beam injected L-mode plasmas on KSTAR *Phys. Plasmas* **23** 052510

[24] Deng B.H., Brower D.L., Cima G., Domier C.W., Luhmann N.C.Jr. and Watts C. 1998 Mode structure of turbulent electron temperature fluctuations in the Texas Experimental Tokamak Upgrade *Phys. Plasmas* **5** 411–4120

[25] Sung C. *et al* 2017 Increased electron temperature turbulence during suppression of edge localized mode by resonant magnetic perturbations in the DIII-D tokamak *Phys. Plasmas* **24** 112305

[26] McKee G.R. *et al* 2013 Increase of turbulence and transport with resonant magnetic perturbations in ELM-suppressed plasmas on DIII-D *Nucl. Fusion* **53** 113011

[27] Kikuchi Y. *et al* 2006 Modelling of the penetration process of externally applied helical magnetic perturbation of the DED on the TEXTOR tokamak *Plasma Phys. Control. Fusion* **48** 169

[28] Heyn M.F., Ivanov I.B., Kasilov S.V., Sergei V., Kernbichler W., Joseph I., Moyer R.A. and Runov A.M. 2008 Kinetic estimate of the shielding of resonant magnetic field perturbations by the plasma in DIII-D *Nucl. Fusion* **48** 024005

[29] Becoulet M. *et al* 2012 Screening of resonant magnetic perturbations by flows in tokamaks *Nucl. Fusion* **52** 054003

[30] Oh Y., Hwang H.J., Leconte M., Kim M. and Yun G.S. 2018 Effect of time-varying flow-shear on the nonlinear stability of the boundary of magnetized toroidal plasmas *AIP Adv.* **8** 025224

[31] Conway G.D. *et al* 2006 Observations on core turbulence transitions in ASDEX Upgrade using Doppler reflectometry *Nucl. Fusion* **46** S799

[32] Conway G.D. *et al* 2004 Plasma rotation profile measurements using Doppler reflectometry *Plasma Phys. Control. Fusion* **46** 951

[33] Hirsch M., Holzhauer E., Baldzuhn J., Kurzan B. and Scott B. 2001 Doppler reflectometry for the investigation of propagating density perturbations *Plasma Phys. Control. Fusion* **43** 1641

[34] Stefanikova E., Peterka M., Bohm P., Bilkova P., Aftanas M., Sos M., Urban J., Hron M. and Panek R. 2016 Fitting of the Thomson scattering density and temperature profiles on the COMPASS tokamak *Rev. Sci. Instrum.* **87** 11E536

[35] Burckhart A. *et al* 2010 Inter-ELM behaviour of the electron density and temperature pedestal in ASDEX Upgrade *Plasma Phys. Control. Fusion* **52** 105010

[36] Laggner F.M. *et al* 2016 High frequency magnetic fluctuations correlated with the inter-ELM pedestal evolution in ASDEX Upgrade *Plasma Phys. Control. Fusion* **58** 065005

[37] Fitzpatrick R. 1993 Interaction of tearing modes with external structures in cylindrical geometry (plasma) *Nucl. Fusion* **33** 1049

[38] McKee G.R., Fenzi C., Fonck R.J. and Jakubowski M. 2003 Turbulence imaging and applications using beam emission spectroscopy on DIII-D *Rev. Sci. Instrum.* **77** 2014–9

[39] Jakubowski M., Fonck R.J., Fenzi C. and McKee G.R. 2001 Wavelet-based time-delay estimation for time-resolved turbulent flow analysis *Rev. Sci. Instrum.* **72** 996–9

[40] Beidler M.T. *et al* 2017 Nonlinear modeling of forced magnetic reconnection in slab geometry with NIMROD *Phys. Plasmas* **24** 052508

[41] Fridström R., Frassinetti L. and Brunsell P.R. 2015 Hysteresis in the tearing mode locking/unlocking due to resonant magnetic perturbations in EXTRAP T2R *Plasma Phys. Control. Fusion* **57** 104008

[42] Van Milligen B. Ph., Hidalgo C. and Sanchez E. 1995 Nonlinear phenomena and intermittency in plasma turbulence *Phys. Rev. Lett.* **74** 395

[43] Diamond P.H., Rosenbluth M.N., Sanchez E., Hidalgo C., Van Milligen B. Ph., Estrada T., Branas B., Hirsch M., Hartfuss H.J. and Carreras B.A. 2000 In search of the elusive zonal flow using cross-bicoherence analysis *Phys. Rev. Lett.* **84** 4842

[44] Wilcox R.S., Shafer M.W., Ferraro N.M., McKee G.R., Zeng L., Rhodes T.L., Canik J.M., Paz-Soldan C., Nazikian R. and Unterberg E.A. 2016 Evidence of toroidally localized turbulence with applied 3D fields in the DIII-D tokamak *Phys. Rev. Lett.* **117** 135001

[45] Wilcox R.S., Rhodes T.L., Shafer M.W., Sugiyama L.E., Ferraro N.M., Lyons B.C., McKee G.R., Paz-Soldan C., Wingen A. and Zeng L. 2018 Helical variation of density profiles and fluctuations in the tokamak pedestal with applied 3D fields and implications for confinement *Phys. Plasmas* **25** 056108

[46] Conway G.D., Fietz S., Müller H.W., Lunt T., Simon P., Suttrop W., Maraschek M., Happel T. and Viezzer E. 2014 Impact of magnetic perturbation coils on the edge radial electric field and turbulence in ASDEX Upgrade *Plasma Phys. Control. Fusion* **57** 014035

[47] Willensdorfer M. *et al* 2016 Plasma response measurements of external magnetic perturbations using electron cyclotron emission and comparisons to 3D ideal MHD equilibrium *Plasma Phys. Control. Fusion* **58** 114004